Deflectometric Measurement of Specular Surfaces

Sören Kammel and Fernando Puente León, *Senior Member, IEEE*

Abstract—**Even small variations of the curvature of a surface may cause malfunction of a part or be perceived as visually unpleasant. However, in the case of specular and painted surfaces, curvature defects can hardly be detected with traditional measurement methods like triangulation or stereoscopy. We describe new strategies to measure the curvature of such surfaces based on deflectometry. This technique mimics the behavior of a human observer by using the object under examination as a mirror. By analyzing its imaging properties, a partial inference on the surface shape is possible. With this approach, much better results can be achieved as compared with triangulation methods. Furthermore, a reliable measurement of defects showing depths of only a few micrometers is enabled.**

Index Terms—**Curvature measurement, deflectometry, inspection, specular surfaces, triangulation.**

I. INTRODUCTION

MANY industrial products feature at least a partially specular behavior, e.g., windshields, lenses, mirrors, dies, molds, and other polished, varnished, or chrome-plated objects. Their quality control requires highly accurate systems for defect recognition and shape measurement. Deflectometry has proven to be a reliable and accurate approach to accomplish these tasks [1].

Humans typically inspect such surfaces visually by analyzing the surrounding reflected in the surface and looking for deformations. Bumps, dents, and waves, which are almost invisible on diffusely reflecting surfaces, can easily be detected if the surface is specular. In this paper, we present a deflectometric measurement method that mimics the behavior of humans and enables to reliably recognize defects of the surface curvature. Moreover, with regard to the detection of such defects, the proposed approach outperforms conventional triangulation methods like fringe projection [2]–[4].

Deflectometry, as is the case with projection techniques, is based on structured light patterns. When a triangulation method like fringe projection is used, the camera is focused on the surface onto which a light pattern is projected, as shown in Fig. 1(a). Due to the parallax of the camera with respect to the projector, the pattern viewed by the camera shows distortions compared to the original pattern [5]. Fig. 1(b) shows how images are formed in the case of deflectometry. The camera views the surface, but it records a reflection of the pattern generated
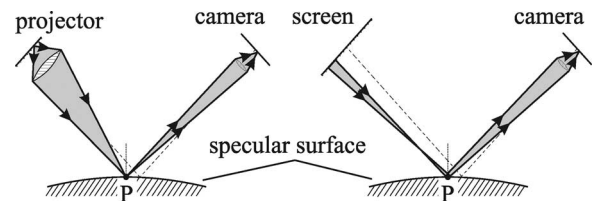

Fig. 1. Measurement principles. (a) Triangulation. (b) Deflectometry.
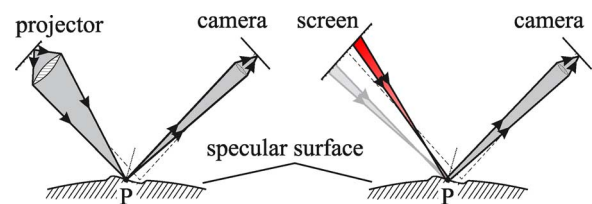

Fig. 2. Sensitivity to the surface slope. (a) Triangulation. (b) Deflectometry.

by the screen. In this configuration, the surface becomes a part of the optical system and, thus, distorts the observed pattern.

Fig. 2 illustrates a difference between the triangulation and deflectometric methods with regard to changes of the surface slope. If the surface is tilted at the point P, the camera still observes the same point of the pattern when projection methods are used, as shown in Fig. 2(a). The same surface characteristic leads to imaging of a completely different area of the screen when deflectometry is employed [see Fig. 2(b)]. In this measurement constellation, the light rays are deviated depending on both the slope and the distance between P and the pattern on the screen.

We will show that the sensitivity of our method with regard to the local surface gradient is roughly proportional to the distance between the surface point P and the screen so that an increase of this distance can be used to enhance its sensitivity [6]. Since the surface is not observed directly, there is a tradeoff between lateral resolution and sensitivity of the method which is balanced by the position of the focal plane of the camera. Focusing on the surface would maximize the lateral resolution of the surface being inspected at the expense of a reduced sensitivity. Focusing on the screen, however, allows the capture of the pattern with the highest resolution possible, but in this case, the surface is out of focus and thus becomes blurred. As will be shown in the next section, by using certain patterns, the focal plane of the camera can be placed close to the surface without significantly sacrificing the sensitivity of the system.

The remainder of this paper is organized as follows. In the next section, the concept of the imaging function is introduced, and a robust method to measure it is proposed. The imaging function describes the local gradient of the surface, and by further processing of these data, the local surface curvature can
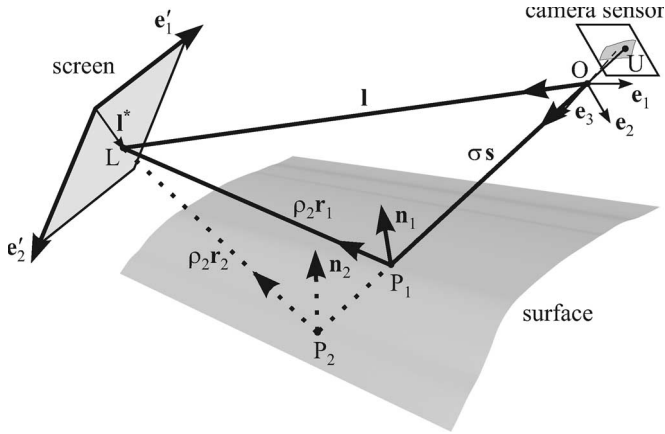
Fig. 3. Optical layout of the system. L denotes a point on the screen, and U denotes the corresponding point on the camera sensor. O is the optical center of the camera. The vectors $\mathbf{e}_1$, $\mathbf{e}_2$, and $\mathbf{e}_3$ define the camera coordinate system, whereas $\mathbf{e}_1'$ and $\mathbf{e}_2'$ refer to screen coordinates. $\mathbf{n}_1$ and $\mathbf{n}_2$ denote normal vectors of the surface. All vectors are unit vectors.

be obtained. Section III presents a strategy to perform a relative measurement of a surface under investigation by comparing its local curvature with a reference. Finally, Section IV presents experimental results and shows that our method features a high sensitivity and allows measuring defects featuring depths of only a few micrometers.

II. PROPOSED APPROACH

A. Imaging Function

Fig. 3 shows the measurement system schematically. The correspondence between the coordinates $\mathbf{l}^* = (l_1^*, l_2^*)^{\mathrm{T}}$ of a point L on the screen given in screen coordinates and the location $\mathbf{u} = (u_1, u_2, -c)^{\mathrm{T}}$ of its image on the camera sensor described in camera coordinates is given by the imaging function

$$\mathbf{l}^*(\mathbf{u}) = (l_1^*(\mathbf{u}), l_2^*(\mathbf{u}))^{\mathrm{T}} \tag{1}$$

where c denotes the distance between the optical center of the camera and the sensor plane. The function $\mathbf{l}^*(\mathbf{u})$ implicitly describes the shape of the surface being measured. Unfortunately, the correspondence between $\mathbf{l}$ and $\mathbf{u}$ is not one-to-one, because for any point along the observation ray $\mathbf{s}$, a surface gradient exists that maps the point L onto the point U. One way to avoid this ambiguity consists in incorporating additional constraints to reduce the number of possible solutions—e.g., to consider sufficiently smooth surfaces only. Our approach, however, is based on performing a relative measurement by comparing the surface under investigation with a reference, as will be described in Section III.

A point P on the specular surface of interest can be described in a local surface coordinate system by a vector consisting of two components v_1 and v_2 parameterizing the surface. In the camera coordinate system, such a point may be identified by the vector $\mathbf{s}$ starting at the optical center O of the camera and pointing away from the direction that is defined by the position vector $\mathbf{u}$. The vector $\mathbf{s}$ is a unity vector which is scaled with the scalar σ describing the distance between the optical center and the surface point P. Since the surface is always described from

the camera view, and the parameterization of the surface can be chosen arbitrarily, the surface parameters are chosen such that they are coupled with the image coordinates

$$(v_1, v_2)^{\mathrm{T}} \overset{!}{=} (u_1, u_2)^{\mathrm{T}}. \tag{2}$$

B. Measurement of the Imaging Function

To measure the imaging function according to (1), we consider an intensity pattern consisting of a single bright point L displayed on the screen, as shown in Fig. 3. The imaging function for this point could, e.g., be measured by detecting the brightest point U in the recorded image and retrieving its coordinates $\mathbf{u}$.

To determine the imaging function for all sensor elements of the camera simultaneously, a large number of more efficient coding schemes exist—e.g., binary codes, discrete-Fourier-transform (DFT) phase demodulation techniques, and Moiré techniques [7]. Unfortunately, most of them are not suitable to perform deflectometric measurements [7].

1) Binary codes, like the Gray code, require the camera to be focused on the screen [8]. Furthermore, even in the ideal case of a perfect optical mapping, only one-to-one correspondences between pixels on the screen and pixels on the camera can be determined. Thus, high-resolution patterns are necessary to achieve a reasonable spatial resolution such that defects can be recognized.

2) Standard DFT phase demodulation techniques typically utilize 1-D patterns and presuppose that the reflected patterns be aligned with them [9]. Unfortunately, this only happens with sufficiently flat surfaces. Two-dimensional DFT phase demodulation methods suffer in a similar manner, if the surface curvature leads to large deformations of the reflected patterns.

3) Moiré techniques are based on the interference of two patterns. They require high carrier frequencies and are thus sensitive to focal blur. Depending on whether the interference takes place optically or in a computer, two cases can be distinguished. Optical Moiré deflectometry requires an alignment to a reference grid or—if using the discrete structure of the sensor itself—a costly system calibration. In the case of numerical Moiré deflectometry, the signal analysis is similar to the DFT phase demodulation. Thus, the same restrictions apply to both methods.

Phase-shifting methods represent a class of coding techniques to which none of these restrictions apply. Together with sinusoidal patterns, high-quality results can be achieved—provided that a suitable decoding and phase-unwrapping method be chosen. The minimum number of phase steps is given by the well-known three-bucket algorithm, but in the case of deflectometry, due to the first-order harmonics introduced by real sinusoidal patterns, the four-bucket algorithm showed to process the data more reliably. For this reason, the four-bucket algorithm was used in the presented system.

However, phase-shifting algorithms have an important drawback. They deliver values limited to the range of one period of the used sinusoidal patterns. Thus, a phase-unwrapping

algorithm is needed. Phase ambiguities caused by discontinuities and noise cannot be resolved in every case. A solution to this problem is to perform the phase unwrapping with information obtained from additional measurements. To retain the advantageous properties of these methods, a second phase image is calculated using a wavelength different to the one used during the first measurement. Unwrapping the phase from the two-wrapped phase images using the Chinese remainder theorem (Nonius principle [10]) produced unsatisfactory results, because the underlying integer arithmetic requires low noise images, as well as nearly ideal sinusoidal patterns. Such patterns, however, are usually not achievable with conventional optical devices.

To compute the phase information more robustly, multiple images of sinusoidal patterns showing different period lengths are recorded and then iteratively fused to the imaging function. The starting period q_1 is chosen large enough to cover the whole measuring range. It delivers a coarse estimate of the phase values without phase jumps. A second phase image is then calculated using a fraction of the starting period length and is subsequently unwrapped using the first image. The unwrapping is done by adding $n \cdot q_2, n \in \mathbb{Z}$ to each point of the second image to ensure that the difference between both images does not exceed the period length q_2 of the second image at any point.

To speed up the unwrapping process and to hide distortions, regions with a low modulation are masked. As a measure of the modulation, the spread of each pixel in the coarse phase image series is used. The fused phase image contains the values of the imaging function according to (1), which is proportional to the local gradient of the surface. Owing to this scalable approach, the accuracy of the measurement system can be adapted to the inspection needs.

C. Postprocessing

Due to the high dynamic range of the phase image, which actually represents screen coordinate values, the imaging function has to be processed for the purpose of defect detection. First, the magnitude of the gradient of the imaging function is calculated using a discrete difference operator. This results in values proportional to the local surface curvature and therefore highlights changes of the surface slope. Subsequently, the reciprocal image is computed to stress the dynamic range of small slope deviations. Prior to this inversion, one is added to avoid divisions by zero. The inverted data are basically proportional to the radius of the local curvature and can be used to perform an automated inspection.

D. Lateral Resolution

Because the used sinusoidal functions are eigenfunctions of the optical system, the camera can be focused on a virtual plane close to the specular surface. This setting was used in our system. The closer the focal plane can be to the surface the higher the surface reflectance is. The achieved lateral resolution is determined by the diameter D_m of the blur spot on the surface that is assumed to be circular (see Fig. 4).
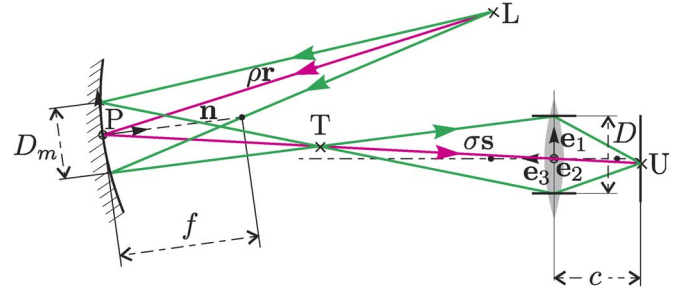

Fig. 4. Optical path of the measurement system. L denotes a point on the screen, P on the specular surface, and U in the sensor plane.

The diameter D_m around a surface point P with a normal vector $\mathbf{n}(\mathbf{u})$ can be approximated as follows: first, the position of the point T is calculated, whose sharp image in the sensor plane is the point U. Then, the normal vector is projected onto the aperture plane of the camera. Next, the two points that result from the intersection of the projected normal vector and the circle of the aperture with diameter D are determined.[1] After this, the projections of these two points onto the tangential plane of the surface point P are calculated using the point T as the projection center. The distance between both points in the tangential planes is an estimate of the blur spot diameter

$$D_\mathrm{m}(\mathbf{u}) \approx \frac{\sigma D}{|\mathbf{n}(\mathbf{u})\mathbf{e}_3|} \cdot \left| 1 - \frac{\sigma V}{\|\mathbf{u}\|} \right| \tag{3}$$

where V is the magnification of the camera. For a derivation and a detailed discussion of this equation, see [11].

E. Sensitivity

Apart from the lateral resolution, sensitivity is one of the most important features to characterize a measurement system. Sensitivity is generally defined as the ratio between the observed magnitude and the magnitude of interest. In the following, the sensitivity of a deflectometric system will be derived with regard to changes of both the shift of a location and its surface slope.

To specify the sensitivity $S(\mathbf{u})$, we shall consider a screen pattern consisting of a single bright point L_1 reflected by the surface under inspection at the point P and viewed by the camera at position $\mathbf{u}$. If the surface point P is shifted or the surface is tilted around this point, not the bright point L_1 but a (dark) point L_2 of the screen will be viewed by very same sensor element of the camera described by the vector $\mathbf{u}$ (see also Fig. 2).

Obviously, the imaging function depends on both the shift of the point P and the surface slope at this very point. The shift $\Delta\mathbf{l}(\mathbf{u}) := \overline{L_1 L_2}$ of the corresponding point of the screen viewed from the sensor location $\mathbf{u}$ represents the observable. Consequently, to investigate the sensitivity $S(\mathbf{u})$ of a deflectometric system, the magnitude $\|\Delta\mathbf{l}(\mathbf{u})\|$ must be determined (see Fig. 5).

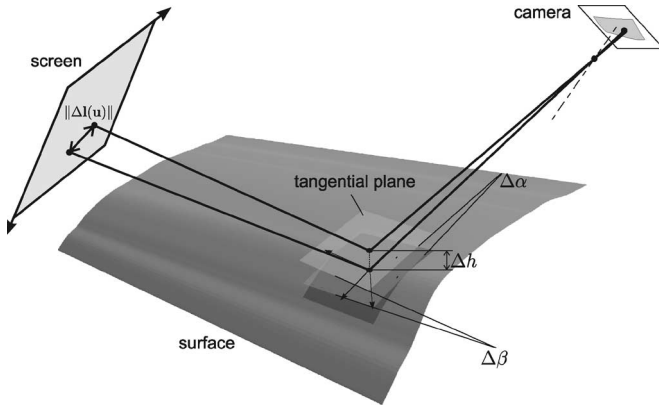[1]This relation can be visualized best in a 3-D view (see [11]).

Fig. 5. Change $\|\Delta \mathbf{l}(\mathbf{u})\|$ of the measured screen position after tilting the tangential plane around a surface point by $(\Delta\alpha, \Delta\beta)$ and shifting it by Δh.

To simplify the description of the sensitivity, a local surface coordinate system spanned by the normal vector at the point P and the vectors parallel and perpendicular to the reflection plane will be used. The screen is assumed to be plane and perpendicular to the reflected observation ray $\mathbf{r}$. A shift Δh only affects the reflected ray if it features a component parallel to the normal vector of the considered surface point. Its contribution to the shift in the screen plane is

$$\Delta l_{\text{shift}} = 2\Delta h \sin\theta \qquad (4)$$

where θ denotes the elevation angle of the incident observation ray. The reflected observation ray is shifted inside the reflection plane if only a shift of the surface point P occurs. The shift increases with the elevation angle θ and thus with a lower angle between surface and the optical axis of the camera. The distance between surface and screen has no effect on the sensitivity if only a shift occurs.

In contrast, a tilt of the surface with an angle $\Delta\alpha$ inside or a tilt with an angle of $\Delta\beta$ perpendicular to the reflection plane results in the following change of position of the observed light source:

$$\Delta l_{\text{tilt},1} = \rho\tan(\Delta\theta)$$
$$= \rho\tan(2\Delta\alpha)$$
$$\approx 2\rho\Delta\alpha \qquad (5)$$
$$\Delta l_{\text{tilt},2} \approx 2\rho\Delta\beta. \qquad (6)$$

If only a surface tilt occurs, the observed change of position of the light source is proportional to the distance ρ between surface and screen. Therefore, the sensitivity can be increased by increasing this distance.

By combining (4)–(6), a measure for the overall sensitivity results based on the overall change of position of the observed light source $\|\Delta\mathbf{l}(\mathbf{u})\|$

$$S(\mathbf{l}) = \|\Delta\mathbf{l}(\mathbf{u})\|$$
$$= \sqrt{(\Delta l_{\text{shift}} + \Delta l_{\text{tilt},1})^2 + \Delta l_{\text{tilt},2}}$$
$$= 2\sqrt{(\rho\Delta\alpha + \Delta h \sin^2\theta)^2 + (\rho\Delta\beta)^2}. \qquad (7)$$

As can be seen in (7), for sufficiently flat surfaces, the sensitivity $S(\mathbf{l})$ of the deflectometric system depends linearly on the distance ρ between the surface and the screen. A sensitivity reduction caused by a simultaneous shift and tilt can therefore only occur inside the reflection plane.

III. COMPARISON WITH REFERENCE OBJECTS

To perform a quantitative comparison with reference objects, an accurate alignment of their corresponding data sets is required. Because an exact positioning of real objects would be too laborious, the alignment takes place in the computer. To this end, corresponding features are extracted from both the object under investigation and the reference object, and these features will be used to align the data sets.

A. Feature Extraction

Suitable features to perform a data alignment are typically extracted from surface regions showing a distinct texture. However, the surfaces under consideration are mostly smooth and untextured. Additionally, not the surfaces are observed directly but the surrounding reflected in them.

Features that are independent of the surface texture and invariant to translation and rotation are the local principal curvatures κ_1 and κ_2 along the principal directions, which can be obtained from the eigenvalues of the Weingarten mapping matrix [12]. Its calculation is simple, because the imaging function already describes the surface gradient. In this case, an approximation of this matrix is obtained from the local structure tensor [12]. To this end, the values of the imaging function are combined according to their contribution to the surface gradient—and, thus, to the local curvature—along the coordinate directions $\mathbf{e}_1$ and $\mathbf{e}_2$

$$\mathbf{m}_{\mathbf{l}^*}(\mathbf{u}) = \left(\text{sgn}\left(\frac{\partial l_1^*}{\partial u_1}\right)\left|\frac{\partial \mathbf{l}^*}{\partial u_1}\right|, \text{sgn}\left(\frac{\partial l_2^*}{\partial u_2}\right)\left|\frac{\partial \mathbf{l}^*}{\partial u_2}\right|\right)^{\text{T}}. \qquad (8)$$

If the screen coordinate system is not rotated more than $90°$ with respect to the camera coordinates, the sign of the local curvature can be reconstructed from the partial derivatives $\partial l_1^*/\partial u_1$ and $\partial l_2^*/\partial u_2$. From the combined curvature values, the structure tensor for a region of radius R

$$\mathcal{U}(\mathbf{u}) := \{\boldsymbol{\xi} | \boldsymbol{\xi} = \mathbf{u} + \boldsymbol{\epsilon}, \|\boldsymbol{\epsilon}\| \leq R\} \qquad (9)$$

is obtained

$$\mathbf{T}(\mathbf{u}) = \int_{\mathcal{U}(\mathbf{u})} (\mathbf{m}_{\mathbf{l}^*}(\mathbf{u}') \times \mathbf{m}_{\mathbf{l}^*}(\mathbf{u}'))\, \mathrm{d}\mathbf{u}$$
$$\approx \begin{pmatrix} \sum_{\mathcal{U}(\mathbf{u})} \mathbf{m}_{l_1^*}^2 & \sum_{\mathcal{U}(\mathbf{u})} \mathbf{m}_{l_1^*}\mathbf{m}_{l_2^*} \\ \sum_{\mathcal{U}(\mathbf{u})} \mathbf{m}_{l_1^*}\mathbf{m}_{l_2^*} & \sum_{\mathcal{U}(\mathbf{u})} \mathbf{m}_{l_2^*}^2 \end{pmatrix}. \qquad (10)$$

The principal curvatures can now be determined by

$$\kappa_{1,2} = \frac{1}{2}\text{trace}\,[\mathbf{T}(\mathbf{u})] \pm \frac{1}{2}\left\{\text{trace}^2\,[\mathbf{T}(\mathbf{u})] - 4\,|\mathbf{T}(\mathbf{u})|\right\}^{1/2}. \qquad (11)$$

The larger eigenvalue corresponds to the maximum local curvature and the smaller one to the minimum local curvature. The principal directions are always orthogonal.

For the alignment to the data set of a reference object, particularly regions with pronounced curvature, values are appropriate, because the confidence of an assignment of these regions to their actual counterparts in the reference data set is very high. Therefore, only regions with a second principal curvature larger than a given threshold s_1 and a principal curvature ratio in the range $s_2 < \kappa_1/\kappa_2 < s_3$ are considered. The second condition assures that sharp contours be excluded from the estimation of the alignment transformation, which may be necessary, if sharp edges with lower quality than the remaining surface appear.

B. Data Alignment

The data alignment assures that only corresponding regions be compared when calculating the deviation between the data of the object under investigation and the reference object. Without a proper alignment, even the wanted curvature of the surface would yield large differences between both data sets.

The shape context descriptor (SCD) was originally proposed for the purpose of shape recognition [13]. It relies on the assumption that the shape of an object can appropriately be represented by its internal and external contours. To represent the contours in a compact manner, a set of vectors is considered, originating from a point $\mathbf{x}_1$ of a contour to all other sample points of the shape. These vectors express the configuration of the entire shape relative to the selected reference point. This point distribution yields a robust, compact, and highly discriminative descriptor. For a point $\mathbf{x}_i$ of the shape, a coarse histogram h_i of the relative coordinates of the remaining $n - 1$ points $\mathbf{x}_j$

$$h_i(k) = |\{j \neq i : (\mathbf{x}_j - \mathbf{x}_i) \in \text{bin}(k)\}| \qquad (12)$$

is computed. This 2-D position histogram associated with $\mathbf{x}_i$ is called the shape context of this point. To make the descriptor more sensitive to positions of nearby sample points, bins that are uniform in log-polar space are used.

SCDs help to incorporate global image properties in the matching process. Additionally, they do not depend on the invariance of pixel intensities but instead only depend on the invariance of relative positions of the feature points. Therefore, shape context matching yields a substantial amount of robustness against image noise.

To align the data, the following 2-D affine mapping $\mathbf{A}$ is performed:

$$\mathbf{u}'_{i,\text{obj}} = \begin{pmatrix} u'_{i,\text{obj},1} \\ u'_{i,\text{obj},2} \\ 1 \end{pmatrix} = \mathbf{A}\mathbf{u}'_{i,\text{ref}}$$

$$= \begin{pmatrix} a_1 & a_2 & a_3 \\ a_4 & a_5 & a_6 \\ 0 & 0 & 1 \end{pmatrix} \begin{pmatrix} u'_{i,\text{ref},1} \\ u'_{i,\text{ref},2} \\ 1 \end{pmatrix}. \qquad (13)$$

$i = 1, \ldots, m$, where m is the number of found correspondences. To accurately estimate the mapping parameters
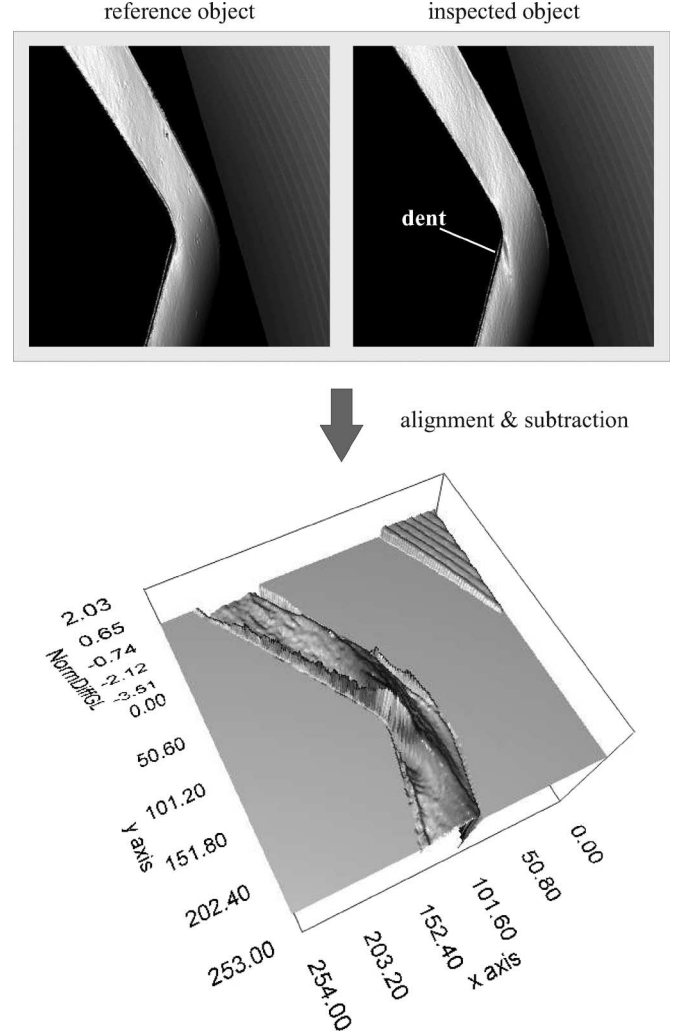

Fig. 6. Defect on the enclosure of a car door window.

$a_1, \ldots, a_6$, typically 500–20 000 point correspondences are necessary. To achieve a robust estimation, a least-median-of-squares approach has been chosen [14], [15]. A subset consisting of three point correspondences is chosen randomly n times ($n > 1000$) from the set of all point correspondences. For each subset, an affine matrix is calculated using a least-squares method. Then, for any of the n estimates of $\mathbf{A}$, the median of the squared distances between the predicted and the measured corresponding points is calculated

$$e_i = \text{med}\left[(\mathbf{A}_i \mathbf{u}_{j,\text{ref}} - \mathbf{u}_{j,\text{obj}})^2\right], \qquad j = 1, \ldots, m. \quad (14)$$

The matrix $\mathbf{A}_i^*$ yielding the smallest error e_i is taken as the best estimate of $\mathbf{A}$. This matrix is applied to the reference image to align it with the measured image, and then, the difference between both images is computed.

Unfortunately, slight differences in the orientation of both objects under comparison cause a nearly constant offset of the gradient data for the whole object data set. For this reason, high-pass filtering is finally applied to the difference image to enhance it. The resulting image describes the location and

reference object   inspected object
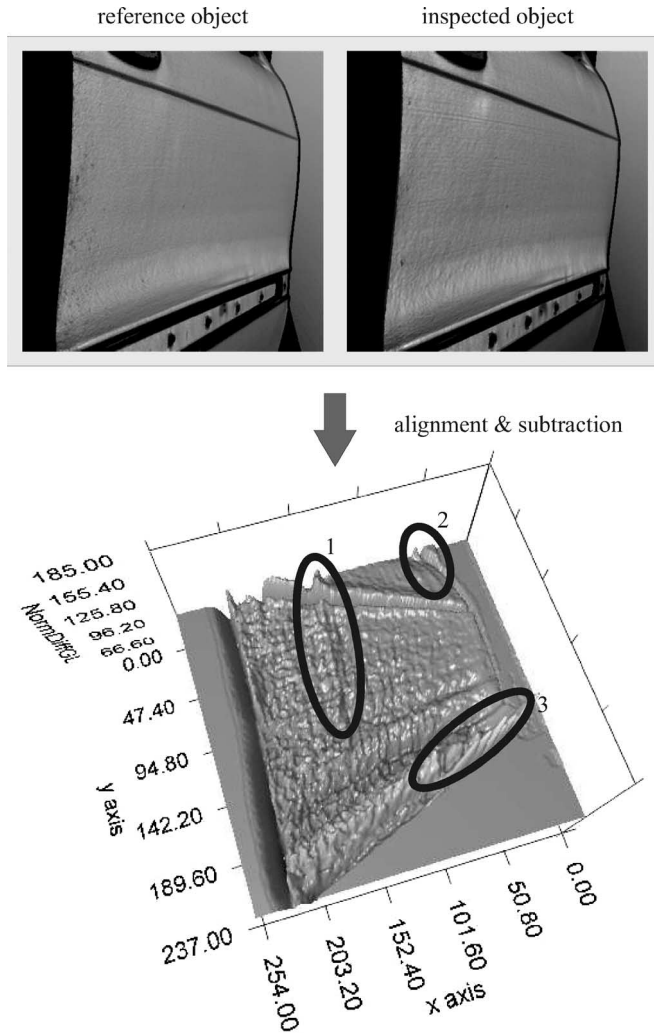

alignment & subtraction

Fig. 7.   Area of a car door with three marked defects.

magnitude of defects in the measured part and can be quantitatively analyzed by means of conventional image processing methods.

IV. EXPERIMENTAL RESULTS

The performance of the method is demonstrated with two painted car doors. Figs. 6 and 7 show the corresponding measured imaging functions, which have been processed as described in Section II-B. The postprocessing weights the defects according to their visibility, because defects on highly curved areas are visually less disturbing than those on flat regions. In Fig. 6, a defect on the enclosure of the window of a car door is depicted. The defect—a dent—would have lead to a rejection of this car door. Fig. 7 shows the measurement result of the central area of another car door. The three marked regions feature defects of different magnitude. The dent beneath the grip tray (marked 1) has a depth of approximately 5–10 μm and can be repaired. The defects next to the fixture of the exterior mirror (marked 2) and to the border of the bumper guard (marked 3), however, are more severe. The insertion beneath the regions 1 and 2 corresponds to a design edge of the door. The values around this edge are very small for two reasons: First, the

normalization based on the local curvature assigns a very small weight to this region, and second, the design edge is produced with a very high accuracy.

In both cases, the comparison of the measured imaging function of a surface with a reference object allows a precise assessment of the surface quality. Since the presented approach mimics the behavior of a human observer inspecting a specular surface, the obtained results match the errors that would be perceived by such an observer.

V. CONCLUSION

The presented deflectometric method utilizes the surface under inspection as a mirror in a known surrounding and achieves a highly accurate measurement of gradient errors. The comparison of the measured imaging function with the data of a reference object allows a precise assessment of the surface quality. Since this approach mimics the inspection behavior of humans, the results match the errors perceived by a human. However, it is often difficult to provide adequate reference objects. A solution to this problem could be based on using computer-aided-design data of the part, which is often available from the product design process.

REFERENCES

[1] S. Kammel and F. Puente León, "Head-mounted display for interactive inspection of painted free-form surfaces," in *Proc. SPIE, Helmet- Head-Mounted Displays VIII: Technol. Appl.*, 2003, vol. 5079, pp. 254–264.
[2] X. Y. Su, W. Zhou, G. von Bally, and D. Vukicevik, "Automated phase-measuring profilometry using defocused projection of a Ronchi grating," *Opt. Commun.*, vol. 94, no. 6, pp. 561–573, Dec. 1992.
[3] R. Furutani, H. Asano, K. Takamasu, and S. Ozono, "3D profile measurement using multi-gray scale compared with reference projections," *Measurement*, vol. 20, no. 2, pp. 129–134, 1997.
[4] P. M. Lonardo, D. A. Lucca, and L. De Chiffre, "Emerging trends in surface metrology," *CIRP Ann.*, vol. 51, no. 2, pp. 701–723, 2002.
[5] B. Denkena, H. Ahlers, F. Berg, and T. Wolf, "Fast inspection of larger sized curved surfaces by stripe projection," *Ann. CIRP*, vol. 51, no. 2, pp. 499–502, 2002.
[6] J. Beyerer and D. Pérard, "Automatische Inspektion spiegelnder Freiformflächen anhand von Rasterreflexionen," *Tech. Mess.*, vol. 64, no. 10, pp. 394–400, 1997.
[7] D. Pérard, *Automated Visual Inspection of Specular Surfaces With Structured-Lighting Reflection Techniques*. Düsseldorf, Germany: VDI Verlag, 2001. Fortschritt-Berichte VDI, Reihe 8, Nr. 869.
[8] G. Sansoni, M. Carocci, and R. Rodella, "Three-dimensional vision based on a combination of gray-code and phase-shift light projection: Analysis and compensation of the systematic errors," *Appl. Opt.*, vol. 38, no. 31, pp. 6565–6573, Nov. 1999.
[9] M. Takeda and K. Mutoh, "Fourier transform profilometry for the automatic measurement of 3-D object shapes," *Appl. Opt.*, vol. 22, no. 24, pp. 3977–3982, Dec. 1983.
[10] K. Ireland and M. Rosen, "The Chinese remainder theorem," in *A Classical Introduction to Modern Number Theory*, 2nd ed. New York: Springer-Verlag, 1990, pp. 34–38.
[11] S. Kammel, *Deflektometrische Untersuchung spiegelnd reflektierender Freiformflächen*. Karlsruhe, Germany: Univ. Karlsruhe, 2005.
[12] G. Farin, *Curves and Surfaces for Computer Aided Geometric Design*. London, U.K.: Academic, 1997.
[13] S. Belongie and J. Malik, "Matching with shape contexts," in *Proc. IEEE Workshop Content-Based Access Image and Video Libraries*, 2000, pp. 20–26.
[14] M. Fischler and R. Bolles, "Random sample consensus: A paradigm for model fitting with applications to image analysis and automated cartography," *Commun. ACM*, vol. 24, no. 6, pp. 381–395, Jun. 1981.
[15] P. J. Rousseeuw and A. M. Leroy, *Robust Regression and Outlier Detection*. Hoboken, NJ: Wiley, 2003.

Sören Kammel was born in Mannheim, Germany, on July 1, 1972. He received the M.S. degree in chemical engineering in 1998 and the Ph.D. degree in May 2004, both from the University of Karlsruhe, Karlsruhe, Germany.

He is currently a Postdoctoral Research Associate at the Institut für Mess- und Regelungstechnik, University of Karlsruhe. His research interests include image processing, automated visual inspection, computer graphics, robotics, and 3-D reconstruction problems.

Fernando Puente León (S'93–M'99–SM'06) received the M.S. degree in electrical engineering and the Ph.D. degree in automated visual inspection from the University of Karlsruhe, Karlsruhe, Germany, in 1994 and 1999, respectively.

He is a Professor with the Department of Electrical Engineering and Information Technology, Technische Universität München, München, Germany. From 2001 to 2002, he was with the Design of Systems on Silicon, Valencia, Spain. From 2002 to 2003, he was a Postdoctoral Research Associate with the Institut für Mess- und Regelungstechnik, University of Karlsruhe, where he was the Head of the Information Fusion Group. His research interests include image processing, automated visual inspection, information fusion, measurement technology, pattern recognition, and communications.